ChemElectroChem

ChemElectroChem

Chemistry Europe
European Chemical Societies Publishing

RESEARCH ARTICLE OPEN ACCESS

Nanostructured Carbon-Enhanced Positive Active Mass for Absorbent Glass Mat 2 V Lead Acid Batteries: Toward Improved Active Material Utilization, Extended Cyclability, and Reduced Water Loss

Marco Cattelan[1] | Giorgia Daniel[2] | Diego Zamboni[1] | Daniele Fabris[2] | Roberto Aliberti[2] | Marco Mazzucato[1] | Silvia Cazzanti[2] | Christian Durante[1]

[1]Department of Chemical Sciences, University of Padova, Padova, Italy | [2]FIAMM Energy Technology S.P.A., Vicenza, Italy

Correspondence: Christian Durante (christian.durante@unipd.it)

Received: 27 December 2025 | **Revised:** 27 January 2026 | **Accepted:** 30 January 2026

Keywords: 50% depth of discharge | absorbent glass mat | lead–acid batteries | sulfation | water loss

ABSTRACT

This article investigates the effects of three commercial carbon compounds—graphite, carbon black (CB), and carbon nanotubes (d-CNT)—on positive active material (PAM) utilization, cycling performance, and water consumption (WC) in 2 V absorbent glass mat lead–acid batteries (LABs). After an initial screening of these materials based on their physicochemical properties—such as surface area, porosity, degree of graphitization, conductivity, and contact angle (wettability)—the carbon additives were incorporated into positive electrodes during manufacturing and tested in cells with a 1+/2− configuration. Both C_{20} and cold cranking tests revealed a significant increase in the specific discharge capacity of LABs containing d-CNT and graphite. Furthermore, LABs incorporating d-CNT or graphite exhibited an enhanced cyclability over other samples during the 50% depth-of-discharge test, also demonstrating a greater capacity to accept a larger charge during initial recharge. WC analysis, conducted in accordance with EN 50 342-1:2016−11 protocol, revealed reduced water loss, particularly in LABs with d-CNT, due to the increased recombination rate of hydrogen and oxygen resulting from electrolyte water electrolysis. Postmortem physicochemical analysis of the positive plates confirms these results. The CB-containing PAM exhibited the highest $PbSO_4$ content, with scanning electron microscopy revealing larger $PbSO_4$ crystallites on its surface. In contrast, graphite- and d-CNT-based samples showed smaller $PbSO_4$ particles randomly distributed over the PAM surface, whereas in the STD PAM, PbO_2 polymorphs covered larger $PbSO_4$ crystallites.

1 | Introduction

Lead–acid batteries (LABs) find applications across various industries, from automotive to telecommunications. Moreover, LABs also play a crucial role in power grids and uninterruptible power supplies [1–3]. LAB technology remains a key player in the global energy storage market, often underestimated compared to the more popular Li-based batteries, thanks to its unique features [4, 5]. Notably, LABs offer several advantages, including a high abundance of lead in the Earth's crust, a cost-effective manufacturing process, and excellent safety features. LABs also boast the highest cell voltage among all aqueous electrolyte systems, operate effectively over a wide temperature range, achieve over 80% of energy efficiency, and have a low self-discharge rate [4, 6, 7]. Furthermore, LABs have a 99% recyclability rate in the US and Europe [7, 8]. Their market, valued at $39 billion in 2018, is projected to reach $94 billion by 2027 [9]. However, significant advancements, particularly in cyclability and durability, are necessary for LABs to compete effectively in the grid storage market [5].

https://doi.org/10.1002/celc.202500472

Over the years, considerable efforts have been made to extend the life cycle of LABs by optimizing the utilization capacity of the PAM, particularly at both low and high discharge rates, which have previously limited their competitiveness [10]. Currently, LABs can achieve only about 40% of their theoretical capacity, in contrast with Li-ion batteries, which can attain 90% [11]. The low cyclability of LABs is closely linked to electrode degradation, caused by the sulfation of the plates and the corrosion of the grids [1, 12, 13]. Sulfation leads to the generation of an insulating layer, composed of large nonconductive $PbSO_4$ crystallites, on the surfaces of both positive and negative electrodes. This hampers electrolyte permeation, thereby decreasing the accessible active mass and ultimately reducing the lifespan of LABs [5]. Conversely, anodic corrosion of the positive grid, driven by the formation of $PbOx\,(1 \le x \le 2)$ and $PbSO_4$ at the interface between the lead grid and the PAM, increases electrical resistance and induces mechanical stress, leading to the development of cracks [12, 14, 15]. Both these issues are closely linked to water loss due to electrolyte water electrolysis, especially during overcharging. Furthermore, the efficiency of the charging–discharging process is dependent on the electrode's active mass, where limited conductivity and mass transfer hamper effective charging and discharging. During *C*-rate discharge operations, the electrolyte often fails to reach the interior of the positive electrodes promptly, causing an abrupt cutoff in the discharge process [16]. This results in a utilization efficiency of the PAM of less than 20% [10]. Additionally, throughout charge–discharge cycles, PbO_2 repeatedly converts to $PbSO_4$ and back, a process involving volume expansion and contraction, contributing to the structural weakening of PAM [5, 12]. To tackle these challenges, carbon compounds have proven effective as additives to enhance the performance of LABs. Currently, various carbon materials, such as activated carbons, carbon nanotubes (d-CNT), and graphite, are used in the negative active material. These compounds improve both capacity and conductivity, while certain crystalline carbon phases enable high-energy density storage. Their incorporation also reduces plate sulfation during discharge cycles, leading to a longer cycle life for LABs without altering the fundamental chemistry of the electrodes [1, 17, 18].

In contrast, research on the PAM is comparatively limited, likely due to the oxidative potential of the plate. However, integrating carbon additives in PAM has shown promising results, particularly in enhancing grid corrosion resistance and improving material utilization.

Shi et al. demonstrated that the addition of rice husk-based porous carbon (RHPC) to positive electrodes improves both electrical conductivity and electron transfer rate, promoting the utilization of PAM. In fact, under 100% depth-of-discharge (DoD) discharge conditions, an increase in discharge capacity by 16% and 23% at 0.05 and 1C was observed in the presence of RHPC [16]. Research by Dada et al. demonstrates that graphene nanosheets, particularly graphene oxide (GO), significantly enhance the capacity utilization of PAM. This enhancement is attributed to increased electrolyte permeation resulting from a rise in preformation porosity. Notably, at a rate of 0.2C, the presence of GO boosts PAM's utilization by nearly 42%, while also improving high-rate performance due to greater reactivity at the graphene/PAM interface [10]. Furthermore, Zhang et al. examined the effects of a synthesized layered Nafion-reduced graphene oxide/polyaniline (HNGP) additive in the PAM of 2 V AGM LABs, focusing in particular on discharge capacity and durability. After formation, an increased α-PbO_2 content was observed in PAMs containing HNGP, which may contribute to longer cell cycle life. In addition, a significant enhancement in discharge capacity was obtained over the 0.05–0.2C rate range [19]. Kosachi et al. examined how expanded and nonexpanded graphite additives influenced the utilization of PAM. They found a direct correlation between total PAM pore volume and utilization across various discharge rates, ranging from 4C to C_{20}. Notably, nonexpanded graphite proved to be a more effective additive than the expanded one in enhancing PAM utilization [11].

The presented work investigated the effect of carbon nanotubes, graphite, and carbon black (CB) on PAM utilization, water consumption (WC), and cycle efficiency. A 2 V AGM–LAB 1+/2− prototype was used to perform the formation and the electrical tests on the homemade carbon-modified positive electrodes. Chemical analyses, including scanning electron microscopy (SEM), X-ray diffraction (XRD), Brunauer–Emmett–Teller (BET), and Hg-porosimetry, were performed postformation to identify potential compositional and morphological differences linked to the presence of carbon in the PAMs. Preliminary electrical tests (C_{20} and CCA) were conducted to investigate the effects of carbon compounds on PAM utilization. Furthermore, 50% DoD cycle tests and WC analysis were done in the same configuration to evaluate their impact on cycling performance and electrolyte water electrolysis. Physical–chemical analyses of the postmortem positive electrodes were performed, along with XRD and surface SEM, to examine the sulfation degree, the ratio of α- to β-PbO_2, and the possible PAMs' morphology differences due to carbon compounds addition.

2 | Experimental Section

2.1 | Carbon Compounds and Their Physicochemical Analyses

Among several carbon-based materials, three different commercial carbon compounds were considered: graphite (Graphite, Imerys), CB (Cabot Corp.), and d-CNT (Black Diamond). These compounds were initially screened based on their physicochemical properties, such as surface area, porosity, degree of graphitization, conductivity, and contact angle (wettability). The selection of these three carbon materials was made because of their clearly distinct properties.

Surface area, pore dimensions, and size distribution were determined by N_2 physisorption (Asap 2020 Plus, Micromeritics). The specific surface area of each sample was obtained by BET analysis and by the quenched solid density functional theory (QSDFT) model, which was shown to be more accurate than the nonlocalized density functional theory method, although limited to a pore dimension of 40 nm. The QSDFT model takes into account the roughness of the surface area and heterogeneity, yielding a better fit to the experimental data, particularly for disordered carbons. The pore size distribution was determined by solving an integral equation in which the experimental data were represented as a convolution of the QSDFT kernel of the theoretical isotherm (calculated for slit, cylindrical, and spherical pores) [15]. The degree of graphitization of each material was determined by Raman spectroscopy and subsequent deconvolution of each spectrum. All the Raman spectra were recorded with a 532 nm laser (30 mW nominal) using a portable device coupled with an optical fiber (BWS465-532H-I Raman Plus, BWTEK-Metrohm Group Company). The electrical conductivity at different compressions was measured by resistance tests on a homemade setup. A PC-controlled press allowed the application of the desired load and read out the resistance/conductivity of the pressed material. The data acquisition system was realized using NI LabVIEW. To evaluate the surface wettability of each carbon, all the measurements were performed in a goniometry configuration. Indeed, the angle was evaluated by taking the tangent of the liquid drop on the surface as observed in a high-resolution image. Table S1 resumes the values of the different properties for each carbon additive.

2.2 | Positive Plate Production

Homemade positive electrodes were produced on a laboratory scale using a procedure developed by FIAMM Energy Technology (FET). The raw materials included lead oxide (PbO), minium (Pb_3O_4), polyester fiber, sulfuric acid (H_2SO_4, 50% vol. solution) and water (H_2O), or water with carbonaceous additives ($H_2O + C$). For the PAM additives, several commercial carbon compounds were selected based on their physicochemical and electrochemical properties, including graphite, CB, and d-CNT. These carbon materials were incorporated into the mixture at $0.04\ \mathrm{wt.\%}_{\mathrm{PbO}}$ during the positive electrode production phase, whereas control standard electrodes were prepared without any further carbon additives (STD) [15]. The paste was then manually spread on the lead grids made of PbSnCa alloy. Each produced plate underwent a curing process in a Memmert HCP50 climatic chamber to achieve a dry electrode, under the procedure established by FET.

2.3 | Absorbent Glass Mat Lead–Acid Battery Cell Prototype Assembly and Formation

A 2 V PVC hermetic AGM prototype cell was assembled with one positive plate and two commercial negative ones [20]. A glass mat acts as the separator, while two polyvinylidene difluoride (PVDF) connectors facilitate the externalization of the electrode terminals. These connectors, crafted from a Pb–Sn alloy, were independently welded to the plates. Electrolyte introduction occurred under vacuum conditions to ensure complete adsorption by the glass mat separator [15]. The required electrolyte volume was determined based on the saturation target and the recorded water loss during preliminary formation. A 10-step constant current procedure was employed for the electrochemical formation, following several preliminary tests on the same prototype cell, with standard commercial electrodes. Each cell was kept in a water bath to maintain a constant internal temperature of 35°C–45°C throughout the formation process, which was performed using a multichannel test system Digatron UBT-ME. Open circuit potential (OCP) and internal resistance (IR) measurements were performed at the end of each battery formation, following a 72-hour rest period, using a Hioki battery tester. Furthermore, the LABs' weight variation observed during the formation, as well as the degree of saturation of the AGM separators, was measured.

2.4 | Preliminary Electrical Tests (C_{20} and CCA)

The preliminary electrical tests were carried out on two other batches of LABs, which were assembled with the same homemade positive electrodes used for the chemical analysis and formed following the same procedure. In the C_{20} tests, each cell was discharged using an I_{20} current, with a cutoff voltage (V_{EOD}) set at 1.75 V, following the EN 50 342-1:2016−11 method. The nominal capacity of the cell was previously determined based on the dimensions of the plates and the average positive active mass. After discharging, the cell was recharged with a constant voltage of 2.67 V for 24 h, limiting the current to $5{\cdot}I_{20}$ (IU charge method). Both the discharge and recharge processes were performed at a temperature of 25°C, utilizing the thermoregulated bath Scientific SC150.

The Cold Cranking Amps (CCA) test was performed on each cell according to the EN 50 342-1:2016−11 method. The cell had to be maintained at −18°C for at least 18 h and then discharged using an I_{CCA} current for 10 s. Subsequently, a rest period of 10 s anticipates a further discharge performed with $0.6{\cdot}I_{\mathrm{CCA}}$ current with a V_{EOD} of 1 V.

2.5 | Life Tests (Water Consumption Test and 50% Depth-of-Discharge Test)

The WC test was conducted following the EN 50 342-1:2016−11 specification for the initial batch of LABs. The test only started after successfully passing the preliminary discharges, which consist of three C_{20} discharges and two CCA. After charging, each battery was cleaned, dried, and weighed (W_i, weight before each step) in grams. The cells were then placed in a thermal chamber, Memmert 600, maintained at 60°C, and charged at 2.4 V for 21 days. Following this overcharge period, each battery was cleaned and dried. 24 h later, the OCP, IR, and weight (W_e, weight after each step) of each LAB were recorded. Subsequently, the cell rested for 8 h at 60°C. The same sequence of operations was repeated on the same LABs three more times for a total experiment duration of 84 days. The weight loss (WL, g/Ah), due to the electrolyte water electrolysis, was calculated after each period of 21 days (Equation (1)), where C_e^{max} is the specific discharge capacity of each cell.

$$WL = \frac{W_i - W_e}{C_e^{max}} \tag{1}$$

The 50% DoD cycle test was conducted on the second batch of LABs that successfully passed a preliminary C_{20} discharge and CCA tests, according to EN 50 342-1:2016−11. Each LAB underwent a series of repeated discharges and recharges. Specifically, the LABs were discharged at a $5{\cdot}I_{20}$ current for 2h to reach 50% DoD, which means LABs were depleted to 50% of their nominal specific capacity. Each discharge was followed by a recharge, during which both the recharge time and the charging factor (CF) were constrained. The CF is defined as the ratio of the specific recharge capacity to the specific discharge capacity. The first charge phase was performed at a voltage-controlled mode for 5 h with a current limit of $5{\cdot}I_{20}$. If a CF of 1.08 was not reached after 5 h, a further charge phase at I_{20} current control mode was done up to reach the desired CF or for a maximum of 1 h. The discharge–recharge cycles were repeated until the end-of-discharge voltage of the tested batteries fell below 1.75 V. The 50% DoD test was carried out by placing each LAB in a water bath maintained at 40°C.

2.6 | Postmortem Physicochemical Analysis of Positive Active Materials after Lead–Acid Batteries' Formation and Life Tests

After the formation process, each cell was dismantled for a chemical analysis of its components. The positive electrodes were thoroughly washed with deionized water and then dried in a convection oven at 60°C. Subsequently, the %PbO_2 content was quantified to evaluate the formation efficiency with a back titration after adding an excess of $Na_2C_2O_4$ in the dissolved sample according to the following reaction

$$5\,C_2O_4^{2-} + 2\,MnO_4^{-} + 16\,H^{+} \rightarrow 2\,Mn^{2+} + 10\,CO_2 + 8\,H_2O \qquad (2)$$

Titration was carried out using the Methrom 905 Titrando automatic titrator. Before proceeding with titration, the sample was dissolved in the attack solution. Furthermore, to investigate the additives' impacts on PAMs porosity, both the Hg-porosimetry and BET analyses were performed on samples collected from the various formed LABs. Specifically, the porosity percentage and intrusion volume were measured using AutoPore IV (9500) Hg-porosimeter, while physisorption isotherms to conduct BET and pore distribution analysis were obtained via nitrogen adsorption–desorption at 77 K using the Micromeritics TriStar II 3020. The surface area was determined from the absorption curve in a multipoint BET analysis ($0.05 < p/p_0 > 0.3$).

Additionally, compositional and structural analyses of various samples were performed through XRD measurements. These analyses were conducted using a Rigaku Miniflex 600 diffractometer equipped with a Cu anode X-ray tube (40 kV, 15 mA), Bragg–Brentano optical module, monochromator, and D/teX Ultra silicon strip detector. Diffraction patterns were collected in the $2\theta = 0°–80°$ range, with $2\theta = 0.02°$ virtual step size, counting an equivalent time of 100 s per step.

SEM analysis was performed using a Thermo-Fisher Phenom XL SEM to investigate the impact of various carbon additives on the structural and morphological properties of the specimens.

After the life tests, each LAB was disassembled for chemical analysis of its components. The positive electrodes were thoroughly washed with deionized water and then dried in a convection oven at 60°C. XRD analysis was employed for the structural and compositional study of the different postmortem plates. To prepare the samples, the active material was extracted diagonally from the plates, starting at the tab and extending to the opposite lower corner, ensuring a representative sample. The material was ground with a mortar and pestle until it became a fine powder. The prepared samples were placed in a PMMA sample holder and loaded into the X-ray diffractometer. X-ray phase analysis was conducted using a Bruker AXS D8 ADVANCE Plus diffractometer fitted with a copper (Cu) source ($\lambda_{K\alpha1} = 1.5406$ Å, 40 mA, 40 kV). The scan range was set between 20° and 80° (2θ) with a step size of 0.03°. The resulting diffractograms were examined using Bruker proprietary software (EVA and TOPAS), alongside the crystallography open database and the specified plate number databases. The phases α-PbO_2, β-PbO_2, and $PbSO_4$ were identified and quantified through Rietveld refinement. SEM analysis was performed on the postmortem positive electrodes to investigate their nano- and micromorphologies. To prepare the samples, a small piece of active material was removed from the grid and mounted onto a SEM sample holder using a strip of carbon tape. Images were captured using a Zeiss Sigma HD FE–SEM, which is equipped with an INCAx-act PentaFET Precision spectrometer (Oxford Instruments). The primary beam acceleration voltages used for imaging ranged from 10 to 20 kV.

3 | Results and Discussion

3.1 | Formation of Various Lead–Acid Batteries With and Without Carbon Compounds

An initial batch of LABs, both with and without carbon compounds in the PAM, was assembled and formed to examine the effects of additives on the structural, morphological, and compositional properties of PAM. Furthermore, two additional batches of LABs, identical to those used for the PAM's chemical analysis, were formed to undergo preliminary electrical tests (C_{20} and CCA) and, later, one of the two was employed for the WC analysis, while the other one to 50% DoD microcycles, respectively. Figure 1a illustrates the potential formation profiles of commercial and homemade standard plates, including those modified with various carbon additives, of LABs subjected to chemical analyses. No significant differences in the shape of the formation profiles are observed between the commercial and homemade electrodes. Only the curve for the cell with CB displays slightly lower voltage during the early stages.

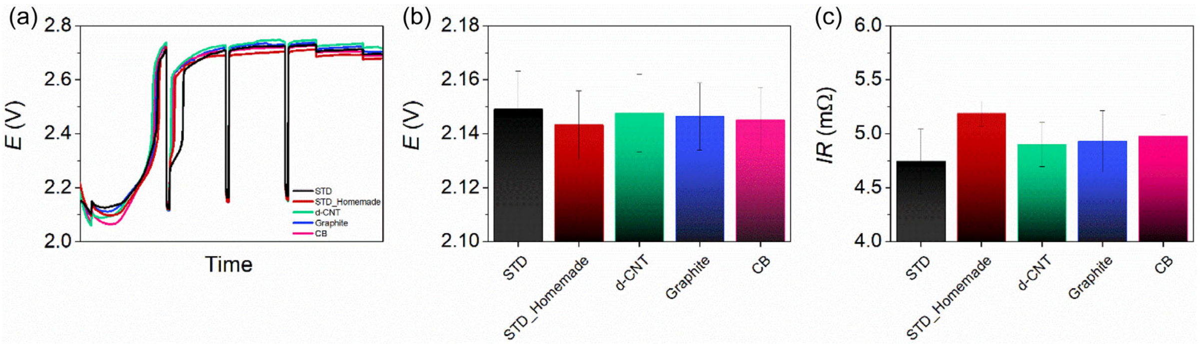

FIGURE 1 | (a) Potential formation profiles for a standard plate, both commercial and homemade, and plates modified with different carbon additives. (b) OCV values and (c) IR values of the different cells formed.

However, the OCP and IR measurements are quite similar, as shown in Figure 1b,c. Both parameters were averaged with those from the cells formed for the 50% DoD and WC tests. As regards each LAB's weight variation associated with electrolyte water electrolysis, the presence of graphite appears to result in a smaller variation, as shown in Figure S1a. In terms of the AGM separator's degree of saturation, no significant differences were observed among the different cells, as shown in Figure S1b. Additionally, all samples display an electrolyte saturation level well above 98%.

3.2 | Chemical Analysis of the Positive Plates After Formation

After the formation resting period, each battery was dismantled for a teardown analysis of the PAM. The amount of PbO_2 was measured to evaluate the formation efficiency. PAM is considered underformed if the PbO_2 content falls below 80%, as suggested by PENOX Gmbh [21]. All cells, except for the one containing CB, displayed an acceptable PbO_2 content, exceeding the threshold value while remaining very close to the reference level, as shown in Figure S2. In the case of the CB cell, the PbO_2 content was slightly lower than the reference. This discrepancy has been attributed in the literature to a slightly higher amount of PbO in the positive cured plate mixture after soaking [22]. During the oxidation of this mixture, comprising $PbSO_4$, 1BS (monobasic lead sulfate, $PbO{\cdot}PbSO_4$), 3BS (tribasic lead sulfate, $PbO{\cdot}PbSO_4{\cdot}H_2O$), Pb_3O_4, and PbO, the PbO is oxidized first, followed by the basic lead sulfates. Consequently, a higher PbO content in that mixture results in a more negative potential for its oxidation to PbO_2 [22]. Lower voltages were recorded during the early stages of the formation step, where the oxidation of PbO to PbO_2 takes place, for this specific cell, as illustrated in its potential curve (Figure 1a). XRD measurements were conducted to determine the crystal phase composition of the PAM from various positive electrodes, as shown in Figure 2a. The spectra revealed three distinct compounds: the α-PbO_2 and β-PbO_2 phases, along with $PbSO_4$. Well-defined peaks characteristic of crystalline materials were observed, with no indications of amorphous phases. Each spectrum displayed four primary peaks at 26° (1 1 0), 32° (1 0 1), 36° (2 0 0), and 50° (2 1 1), which are associated with plattnerite (β-PbO_2). A peak corresponding to scrutinite (α-PbO_2) appeared at 28° (1 1 1), while the peaks for $PbSO_4$ were challenging to identify due to their significantly lower intensities compared to those of the

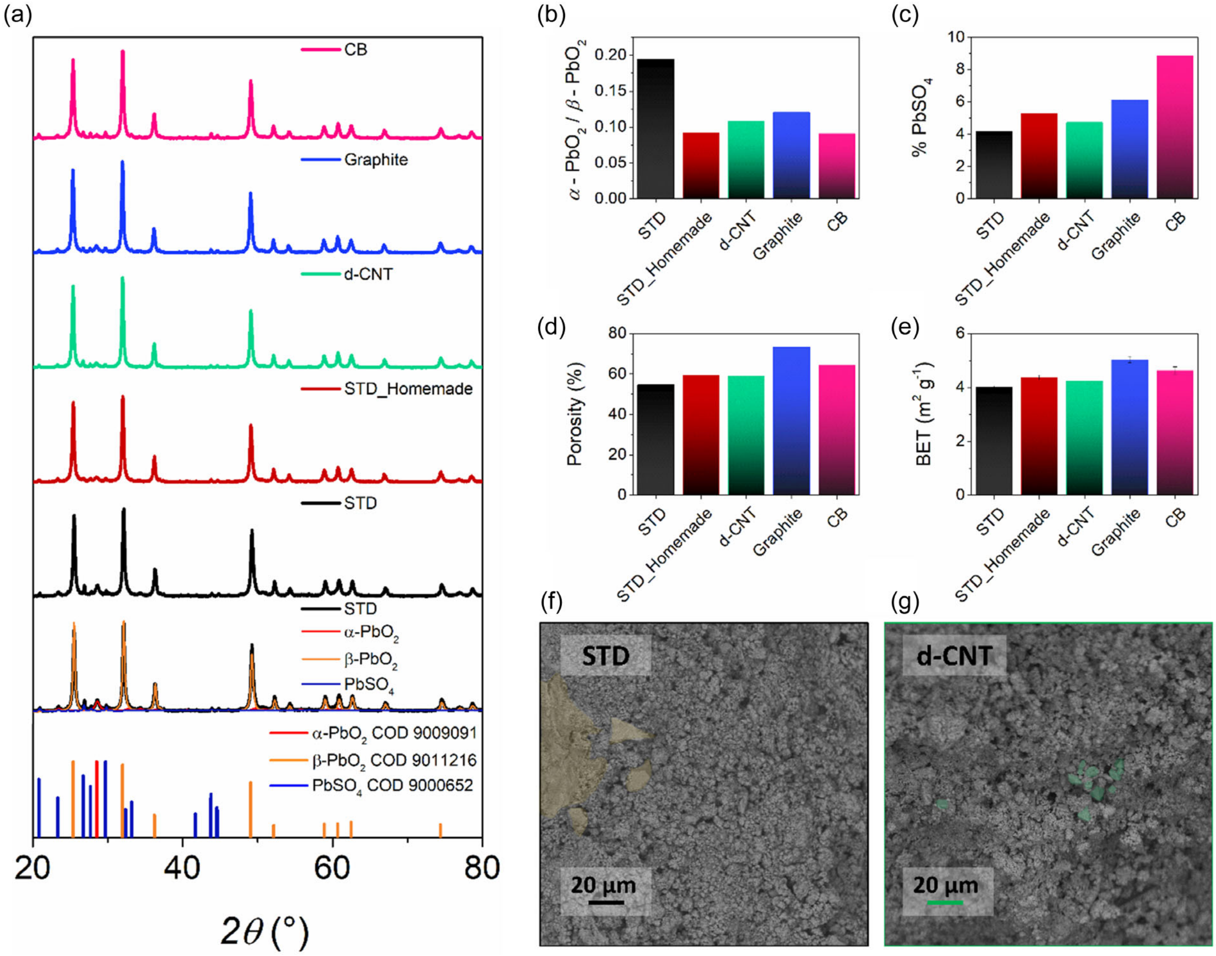

FIGURE 2 | (a) XRD patterns of the post-formation positive electrodes, (b) α-PbO_2/β-PbO_2 ratio, (c) $PbSO_4$ content of various PAMs, (d) porosity and (e) surface area (BET) of the different postformation positive electrodes, SEM images of (f) a formed commercial positive plate without carbon additives and of (g) a homemade formed positive plate with d-CNT in concentration $0.04\%_{\text{wt.PbO}}$. XRD = X-ray diffraction; PAM = positive active material; BET = Brunauer–Emmett–Teller; SEM = scanning electron microscopy.

PbO_2, as noted in the same figure. A Rietveld analysis was conducted on each spectrum to determine the ratios of the alpha and beta phases of PbO_2, as well as the $PbSO_4$ content (see Figure 2b,c). Figure 2b illustrates significant differences in the lead dioxide composition between cells with commercial and homemade plates. The α- to β-PbO_2 ratio may significantly influence LABs' performance. A higher value may lead to a longer cycle life since α-PbO_2 has a lower utilization coefficient than β-PbO_2, which provides a more robust structural framework. However, the extent of this advantage largely depends on the production, curing, and formation processes of the plates themselves [22–24]. No significant differences were noted between the homemade PAMs, with any minor variations observed likely attributed to tool inaccuracies, as shown in Table S2. In terms of $PbSO_4$ content, the cell labeled CB shows the highest amount. This is attributed to the lower quantity of PbO_2 generated during its formation. Conversely, the PAM containing d-CNT exhibited a $PbSO_4$ level similar to the STD sample (Figure 2c). However, from a morphological perspective, the shapes and sizes of $PbSO_4$ crystals generated in these samples differed, as shown in Figure 2f,g. In the STD PAM, large sulfate crystallites covered the surface nonhomogeneously. In contrast, the addition of d-CNT results in the formation of uniformly distributed and significantly smaller $PbSO_4$ particles. This is because carbon nanotubes create well-distributed networks that facilitate a uniform current distribution throughout the plate, promoting the formation of the active material and favoring the nucleation of small $PbSO_4$ crystals [23]. Regarding the two standard PAMs, both samples exhibited similar structure, although the homemade one was slightly less compact (see Figure S3a). The introduction of graphite resulted in a greater open structure (see Figure S3b), likely due to its oxidation during the formation process [22, 25]. Additionally, its presence promoted a more expanded structure through intercalation into the PAM, as shown in Figure S3b [23]. Unlike the STD sample, large sulfate crystallites were absent in both specimens containing graphite and CB (see Figure S3). Hg-porosimetry measurements confirmed a significant increase in PAM porosity with the incorporation of graphite, as shown in Figure 2d. This figure also suggests that CB affected this property, although its influence is not easily discernible from the SEM image. The literature indicates that CB experiences a 60 % weight loss due to oxidation during formation, contributing to the increased PAM porosity and affecting its chemical, physical, and electrical properties [23, 26, 27]. These findings suggest that the presence of dense crystal packing within the plate results in thinner pore structures compared to those observed when graphite is added. Additionally, similar outcomes were obtained from the BET analysis of the same samples. As shown in Figure 2e, the PAM containing graphite has the highest surface area, yet all homemade samples exhibit greater BET values than the STD one. This indicates that the electrode's manufacturing process plays a key role in influencing this parameter, as suggested in the literature [3].

3.3 | Preliminary Electrical Tests (C_{20} and Cold Cranking Amps)

The preliminary electrical tests (C_{20} and CCA) were performed on both batches of LABs, which were then subjected to life tests to assess PAM utilization and to investigate the effect of various additives on it. As regards the C_{20}, each LAB was discharged at a constant current I_{20} until it reached a cutoff voltage of 1.75 V. Figure 3a illustrates the C_{20} curves of the LABs tested for WC. In addition, Figure S4 displays the discharge curves of the second and third C_{20} sequences performed on the same cells, alongside those of the 50% DoD cycle test batteries. All the curves were normalized to the end of the discharge time of the respective reference. The specific discharge capacity of each tested LAB was then determined and normalized based on the specific discharge capacity of the reference one from the same C_{20} sequence. For the first C_{20} analysis, an average value is given, regardless of further tests (see Figure 3b). The same figure shows that the presence of carbon compounds, regardless of their nature, did not lead to improvements in PAM utilization during the first C_{20} sequence. Actually, the incorporation of CB even decreases it, although this may be due to a lower content of PbO_2 generated during the formation process. Conversely, as the cycles progress, a notable enhancement in the utilization of PAM is observed in LABs containing d-CNT and graphite. These results closely match the greater electrical conductivity of d-CNT and graphite compared to that of CB, as shown in Table S1. Consequently, both the compounds, in addition to increasing the PAM's electrical conductivity, promote a uniform charge distribution across the electrode surface. This favors the nucleation of smaller $PbSO_4$ crystals, preventing the accumulation of larger particles that are challenging to reconvert back to PbO_2. Moreover, large $PbSO_4$ crystallites can generate a compact and insulating layer, which hinders the diffusion of the electrolyte through the PAM, increases the Ohmic resistance, and ultimately causes the cell to shut down [23, 25]. Notably, during both the second and third discharges, the highest capacity was recorded by LABs containing d-CNT. This is attributable to the higher wettability of this compound compared with the other two carbon allotropes (see Table S1) and, consequently, to the greater permeation of electrolyte through the PAM. Furthermore, the result obtained due to d-CNT incorporation aligns with what has been observed in the literature [15].

After the initial C_{20}-recharge cycle, both batches of LABs underwent a CCA test. The CCA curves for the LABs designated for the WC analysis are shown in Figure 3c. An additional CCA was conducted on these cells following the completion of the second C_{20}-recharge cycle, unlike the batch intended for the 50% DoD microcycles, which underwent only one CCA (Figure S5). Each curve was normalized based on the CCA end time of the respective reference and can be divided into two sections (Figure 3c). The first part displays the discharge behavior of each LAB, resulting from the application of an I_{CCA} current for 10 s, with the cutoff voltage recorded. Ten seconds after the conclusion of the first part of the test, a second discharge was performed, on each battery, by applying a current of 0.6 I_{CCA} until reaching the cutoff voltage of 1 V (Figure 3c). Both aspects depend on the IR of each cell. However, no significant differences in discharge curve shapes or cutoff voltages were observed among the different LABs. This further confirms that incorporating carbon compounds into the PAM does not alter the IR of the electrode materials during formation or subsequent electrical tests. Figure 3d indicates that cells with the best performances in both CCA tests contain d-CNT or graphite, further confirming the positive impact of these additives on the utilization of the active mass. Notably, the specific discharge capacity of the LAB containing graphite was the highest across both CCA cycles.

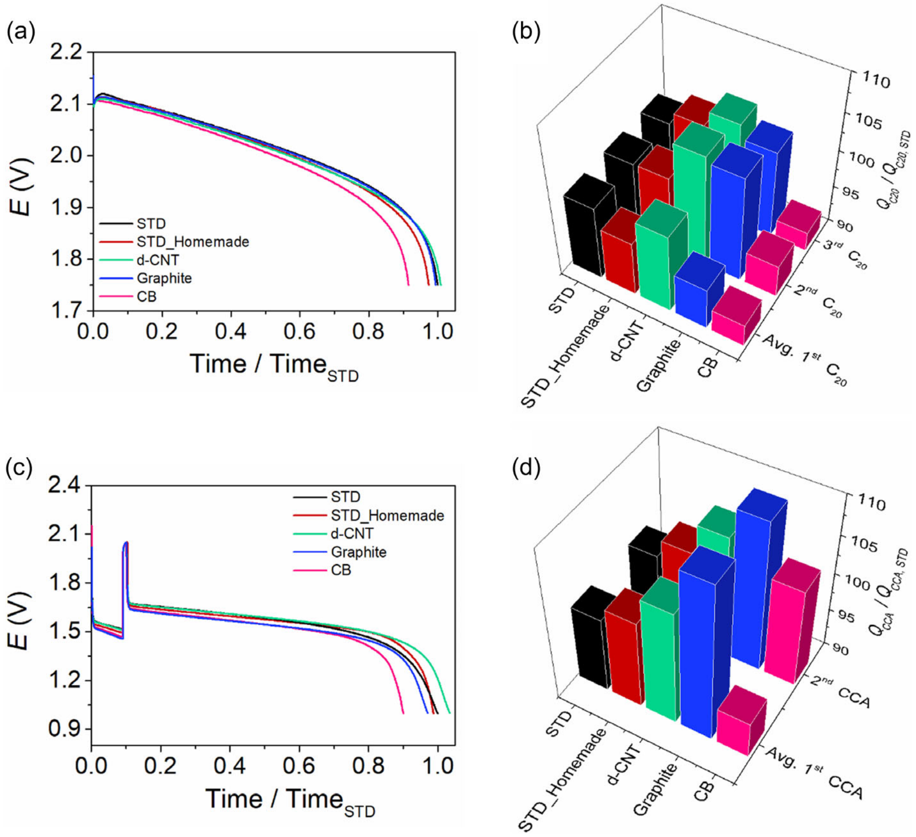

FIGURE 3 | (a) C_{20} curves, (b) results of the specific discharge capacity tests, (c) CCA curves, and (d) data from specific capacity tests of the different cells with or without carbon nanostructured materials in the PAM. The end-of-discharge time for each tested cell was normalized to that of the STD, for both the C_{20} and CCA. Each sequence of capacity data was normalized to the STD of the corresponding sequence for both types of tests.

Moreover, its capacitive behavior remains consistent from one cycle to the next. This likely results from increased PAM conductivity in the presence of graphite, which has higher electrical conductivity and a greater degree of graphitization than the other two carbon allotropes, as shown in Table S1. Additionally, its ability to act as an electro-osmotic pump promotes the electrolyte's permeation through the oxidation-generated pores, leading to more efficient and uniform chemical reactions [23, 25]. In contrast, cells with CB exhibited a specific discharge capacity significantly lower than that of the reference cell at the end of the first CCA. However, during the second CCA, its capacity increased substantially, reaching levels comparable to the STD cell. This enhancement likely results from the oxidation of CB to CO_2 during electrical testing, which increases the porosity of the active material and improves electronic exchange between the PAM and the electrolyte [23, 27]. Nonetheless, its impact on the investigated parameter was considerably less than that of the other two carbon materials.

3.4 | Life Tests (Water Consumption Test and 50% Depth-of-Discharge Test)

After completing the preliminary electrical tests, the two batches of LABs underwent life tests to evaluate the impact of various carbon compounds on each battery's lifespan. During the initial electrical tests, LABs designated for the 50% DoD cycle test were subjected solely to a C_{20}, followed by a CCA. In contrast, the cells used to assess WC underwent three C_{20} and two CCA tests, performed in an alternating sequence. Regarding the life tests, LABs designated for the 50% DoD test were first discharged to 50% of their nominal capacity. Subsequently, multiple discharge and recharge cycles were conducted until the cells shut down. The test was terminated if the cell's voltage fell below the threshold potential of 1.75 V. Figure 4a shows the life cycle curves of the different LABs undergoing the 50% DoD test. It is evident from the same figure that the cyclability of the STD LAB was lower than that of carbon-based cells, except for the CB sample. Despite the STD PAM containing the highest α-PbO_2 level (see Table S2), which provides superior structural and mechanical properties essential for preventing the softening and shedding of active material from electrodes during cycling tests, its performance was significantly inferior to both graphite and d-CNT-incorporating LABs. Notably, the influence of the d-CNTs on cycling performance is particularly pronounced. Their high wettability (see Table S1), combined with their ability to self-organize within the PAM, creating uniform and well-distributed local networks, results in an even distribution of current, which enhances their electrical conductivity and improves the efficiency of conversion reactions [1, 6, 23]. Furthermore, their presence promotes the generation of a compact and well-defined corrosion layer around the grid-cross section, which facilitates adhesion between the PAM and the grid, thereby optimizing the current circulation [15, 28]. Regarding graphite-containing cells, the enhanced cyclability observed is

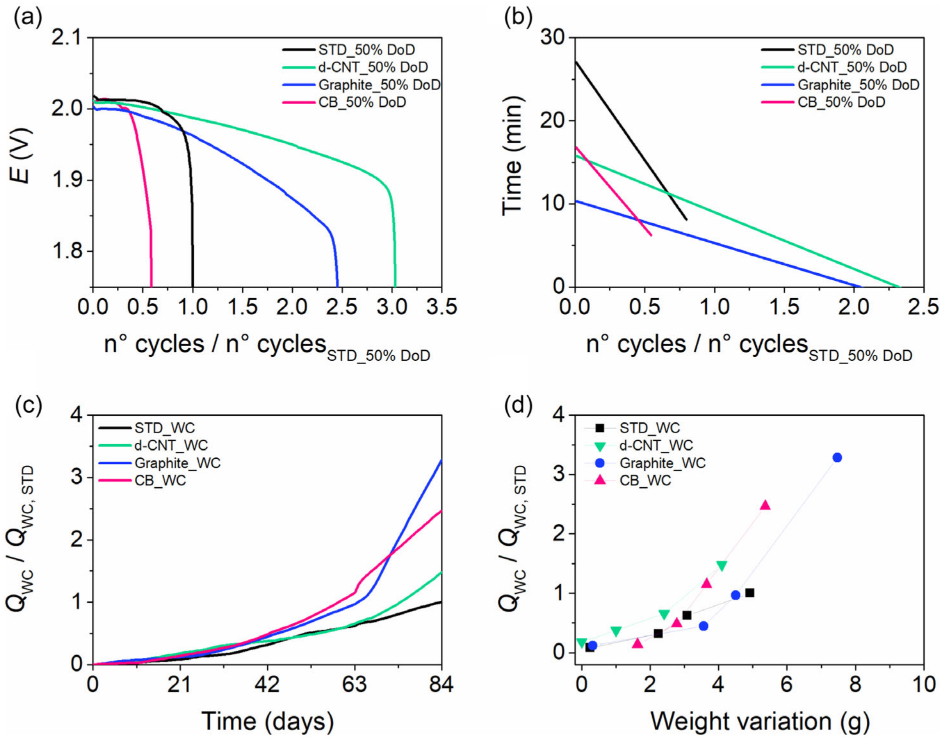

FIGURE 4 | (a) 50% DoD microcycles samples curves; (b) Linear interpolation of the second recharge's time as a function of the cycle numbers; (c) Absorbed capacity (Q_{WC}) curves of the different WC tested samples; (d) Q_{WC} as a function of weight variation for the different cells intended for WC evaluation.

likely attributed to the increased PAM porosity (see Figure 2d,e) and improved interconnections through small pores, thus enabling better-conducting networks with the available PbO_2 particles. Moreover, its role as an electro-osmotic pump aids in the transport of electrolytes through the porous electrode, limiting the concentration polarization and promoting more effective and uniform chemical reactions [23, 25]. In contrast, the least-performing LAB was the one with the CB. Figure 4b illustrates the trend of the time for the second charge phase of the 50% DoD test concerning the number of cycles. Both the curves for the STD LAB and the one containing CB intersect the time axis at higher values than the other two samples tested. The PAM that includes graphite and the one that incorporates d-CNT can accept a larger charge during the first recharge phase. This can be attributed to a better, more uniform, and more effective distribution of the current, as well as the formation of smaller sulfates—which are easier to reconvert—resulting from the addition of these highly electrically conductive carbon compounds. Furthermore, the duration of the second recharge, which follows the first, is short enough to achieve the predetermined charge factor. The slopes of these curves also vary significantly. Notably, the curves for the STD cell and the one labeled CB_50% DoD are nearly parallel and exhibit a considerably steeper slope than the other two samples. A steeper slope indicates a higher degradation rate for the PAM. Both of these cells reach the cutoff potential after completing far fewer cycles than the other two LABs tested. Regarding the LABs used for the WC analysis, each cell was recharged with a constant voltage step for 21 days, while limiting the current to $5 \cdot I_{20}$. After this period, the WL of each cell was measured and normalized based on each cell's specific discharge capacity. The entire experiment, conducted at a temperature of 60°C, spanned a total of 84 days and involved four steps. Figure 4c illustrates the capacity absorbed (Q_{WC}) by each cell throughout the 84-day analysis period. In the initial phase, the Q_{WC} was quite similar across all tested samples, indicating uniform WL for all LABs. However, after 21 days, the trends of the different curves began to diverge significantly. Notably, cells containing graphite or CB exhibited a marked increase in the slope, demonstrating a significantly higher Q_{WC} than the other cells throughout the entire experiment. The impact of d-CNT on the investigated phenomenon was similar to that of CB or graphite during the first half of the test, resulting in a greater Q_{WC} compared to the STD. Subsequently, the curve for the same cell aligned closely with the STD, increasing in slope during the final time interval, as shown in Figure 4c. Figure 4d shows that the charge absorbed during the first 21 days was similar across all cells. Additionally, all LABs experienced minimal weight variation due to electrolyte water electrolysis during this period, except for the battery incorporating CB, which is visible by comparing the very first points for each battery in Figure 4d. The figure also indicates a direct proportional relationship between the Q_{WC} of each cell and the weight variation observed 42 days after the test began. Both graphite-containing and CB-containing LABs demonstrated the highest weight change and Q_{WC} after this time. In contrast, while the presence of d-CNT resulted in a greater Q_{WC} throughout the entire experiment, it also yielded a lower weight variation compared to the STD at each 21-day interval. These findings may be attributed to the increased recombination rate of hydrogen and oxygen resulting from electrolyte water electrolysis, consistent with observations in the literature [15].

3.5 | X-Ray Diffractometry Analysis

Structural and compositional analyses of postmortem positive plates were performed through XRD measurements. The XRD patterns of different samples collected from each electrode after the life tests are shown in Figure 5a, revealing the presence of α-PbO_2, β-PbO_2, and $PbSO_4$ phases. These phases were quantified through Rietveld refinement, and the ratio between the two PbO_2 polymorphs was determined. Notably, the STD PAM exhibited the highest ratio, as shown in Figure 5b. Even after formation, the same sample contained the greatest amount of α-PbO_2 polymorph, along with a consistent content of $PbSO_4$ (see Figure 2b,c). However, following the electrical tests, an approximate 8% reduction in this ratio was observed, significantly exceeding the variation seen in other samples. Throughout the life cycle of LABs, the content of α-PbO_2 gradually diminishes while that of β-PbO_2 increases [2]. This transition affects the structural properties of the PAM, as smaller β-PbO_2 particles potentially may lead to softening and shedding of active material in the positive electrode [13, 23]. As a result, during the 50% DoD test, the performance of the STD LAB was notably poorer compared to both cells incorporating graphite and d-CNT, which exhibited less variation in PbO_2 polymorph composition. Furthermore, a smaller variation in this ratio may also correspond to a smaller change in the volume of the PAM during testing. This is likely due to the reduced transformation between the two different polymorphic phases of PbO_2, which helps maintain greater structural integrity of the PAM. Interestingly, although the LAB with the poorest cyclability, i.e., the one with CB, shows a smaller variation in this ratio compared to those with the other two carbon materials, it is evident that this PAM has the highest amount of $PbSO_4$, as shown in Figure 5c. The presence of a greater amount of $PbSO_4$ crystallites already at the end of formation contributes to the formation of a thick insulating layer. This layer reduces the active surface area between PAM and electrolyte, adversely affecting the structural and mechanical properties, and thus decreasing the LAB's life cycle [12, 29]. Nevertheless, it is also interesting to note that the increase in sulfate content is similar to that observed with the other two carbon additives and remains significantly lower than in the STD.

This further supports the ability of nanocarbons, particularly graphite and d-CNT, to inhibit excessive growth of $PbSO_4$ crystals and mitigate "hard sulfation," thereby increasing PAM porosity and conductivity, due to their intrinsic properties (see Table S1), which in turn improves overall LAB performance.

3.6 | Scanning Electron Microscopy Analysis

SEM analysis was performed on each sample after the life test to examine its surface morphology, as shown in Figure 6. The characteristic "needle-like" and tetragonal crystal structures associated with the α- and β-phases of PbO_2 are observed across all samples [23, 28]. However, their content is notably higher in STD, as shown in Figure 6a,a', further supporting the observations from the XRD analysis. Additionally, both PbO_2 polymorphs uniformly cover the underlying $PbSO_4$ crystallites, interconnected to form a compact structure similar to that observed at the end of the formation process (Figure 2f). Generally, "hard sulfation" mainly affects the negative active mass because the particles have a lower specific surface area (SSA of 0.5–1 m^2 g^{-1}) compared to the PAM (SSA of

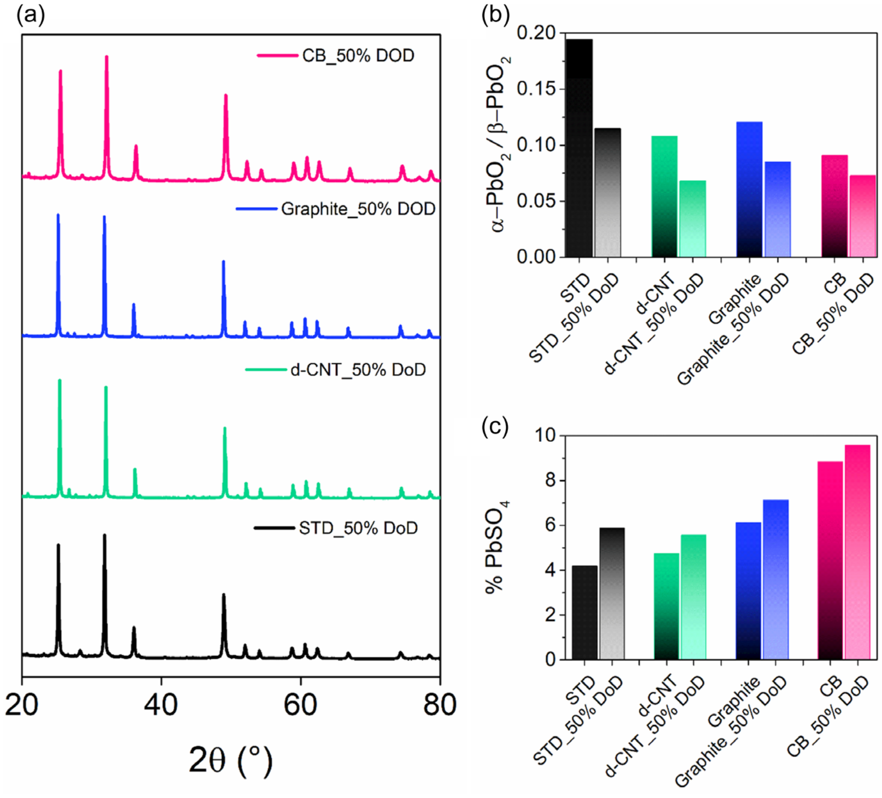

FIGURE 5 | (a) XRD patterns of the postformation positive electrodes; (b) α-PbO_2/β-PbO_2 ratio, (c) $PbSO_4$ content of various PAMs. XRD = X-ray diffraction; PAM = positive active material.

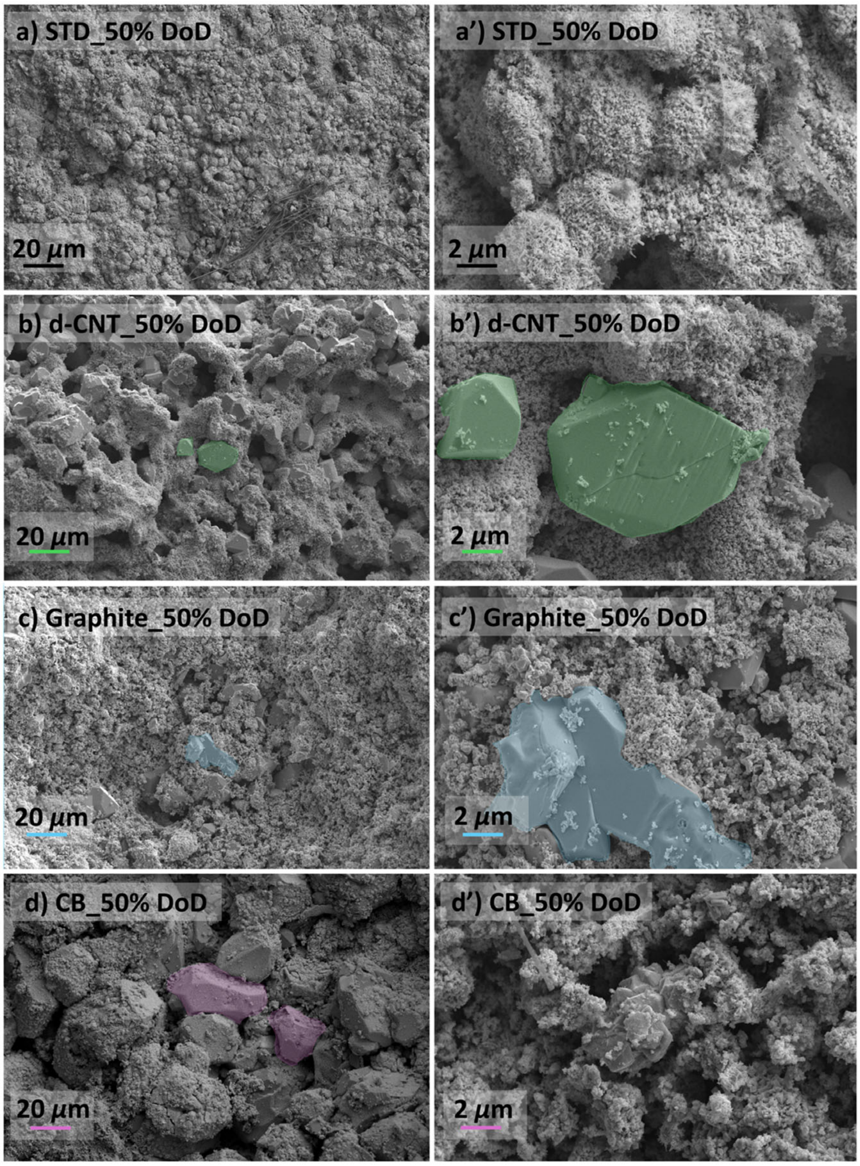

FIGURE 6 | SEM images of a positive commercial standard (a,a') and homemade electrodes modified with carbon additives: d-CNT (b,b'), graphite (c,c'), and CB (d,d'). Right: magnified views of the images on the left. SEM = Scanning electron microscopy; CB = carbon black; d-CNT = carbon nanotubes.

3.0–8.0 $m^2\ g^{-1}$) [4]. However, in batteries subjected to frequent discharge/recharge cycles, such as the 50% DoD test, as well as deep discharges and incomplete recharges, hard sulfation is also evident in the PAM [14]. In fact, from Figure 6d, larger $PbSO_4$ crystallites are visible, forming an insulating and dense coating. This layer, made up of particles of different shapes and sizes, uniformly covers the surface of the PAM. As a result, electrolyte diffusion is hindered, reducing electronic exchange and ultimately shortening the battery's cycle life. Compared to the STD sample, the one containing CB shows a higher $PbSO_4$ content even at the end of its formation (see Figure 2c). As the electrical tests progressed, the crystallization of $PbSO_4$ produced the thick layer shown in Figure 6d, originating from non-solubilized crystallites. Moreover, unlike the STD sample, PbO_2 particles are not evenly distributed across the entire $PbSO_4$ crystallite surfaces, as shown in Figure 6d'. Conversely, in Figure 6c, small $PbSO_4$ particles are distributed randomly on the PAM's surface. The oxidation process involving graphite during formation and electrical testing increases the porosity and surface area of the active material (see Figure 2d,e), improving electrical exchange due to enhanced electrolyte diffusion [23, 25]. This, coupled with increased electrical conductivity from the presence of graphite (see Table S1), promotes the formation of small $PbSO_4$ crystals rather than large particles accumulating on the plates, as seen in the CB sample. A similar outcome was observed when adding d-CNT, as shown in Figure 6b. Although this sample appears more sulfated than the one with graphite (see Figure 6c), XRD analysis suggests the opposite. It is also noted that some $PbSO_4$ particles are covered by PbO_2 crystallites. Additionally, in terms of size, the $PbSO_4$ crystals in both samples are comparable, as shown in Figure 6b',c'. The nucleation of small $PbSO_4$ particles in the PAM is attributed to the presence of d-CNT, which, due to its high wettability and electrical conductivity (see Table S1), enhances electronic exchange between the PAM and the electrolyte, thereby promoting the conversion reaction.

4 | Conclusion

This article investigates the impacts of three carbon compounds: graphite, carbon black, and carbon nanotubes, on the performance of 2 V AGM LAB prototypes. The study specifically evaluates their effects on PAM utilization, cycling performance, and WC when incorporated at a concentration of 0.04 wt.%$_{PbO}$ into the positive electrodes. Preliminary electrical tests (C_{20} and CCA) indicated a significant enhancement in the specific discharge capacity of LABs containing d-CNT and graphite. This improvement is linked to the higher porosity and larger surface area of PAMs, as well as the reduced $PbSO_4$ crystallite size formed on their surface, confirmed by chemical analysis of PAMs after formation. Notably, the addition of carbon materials, apart from CB, did not significantly alter the formation curves, the OCP, or the IRs. In contrast, the cell containing CB recorded lower voltages during the early stages of its formation, as illustrated in its potential curve. This is attributable to a higher PbO content in the mixture after soaking, resulting in a more negative potential for its oxidation to PbO_2.

Regarding cyclability, LAB containing d-CNT demonstrated a significant enhancement compared to the STD LAB during the 50% DoD test. Additionally, the presence of the same compound in LABs subjected to WL analysis resulted in a greater Q_{WC} throughout the experiment, while simultaneously reducing WL compared to the STD at each 21-day interval. This may be attributed to the increased recombination rate of hydrogen and oxygen, produced in overcharging. Conversely, a direct proportional relationship between the Q_{WC} and the WL was noted in other LABs, particularly 42 days after the test began.

The physical–chemical analysis of the postmortem positive electrodes further supports these findings. Notably, XRD measurements indicate an approximate 8% reduction in the ratio between α- and β-PbO_2 of STD PAM subjected to the 50% DoD test, significantly exceeding that observed in other samples. This transition affects the structural properties of the PAM. Consequently, this results in poorer cyclability for LABs compared to those incorporating graphite and d-CNT, which exhibited less variation in PbO_2 polymorph composition. Interestingly, while the PAM collected from the LAB with the poorest cyclability, containing CB, showed a smaller variation in the α- to β-PbO_2 ratio compared to PAMs with the other two carbon additives, it had the highest amount of $PbSO_4$. Furthermore, the larger $PbSO_4$ particles detected in this sample by SEM analysis are challenging to dissolve in the electrolyte and convert back to PbO_2 during the LAB's life span. In contrast, smaller $PbSO_4$ particles were found dispersed randomly on the PAM surfaces in the samples containing graphite and d-CNT, unlike the STD PAM, where larger $PbSO_4$ particles are covered by the PbO_2 polymorphs.

Acknowledgments

We gratefully acknowledge the University of Padova for the financial support through a UNIMPRESA Grant (project number: DAMA2021). Project funded by the European Union—NextGenerationEU—National Recovery and Resilience Plan (PNRR)—Mission 4 Component 2 Investment 1.3—Notice N. 341 del 15.03.2022 of the Ministry of University and Research. XRD Bruker AXS D8 ADVANCE Plus diffractometer at the PanLab department facility was founded by the MIUR- "Dipartimenti di Eccellenza" grant NExuS.

Open access publishing facilitated by Universita degli Studi di Padova, as part of the Wiley - CRUI-CARE agreement.

Funding

This study was supported by the Università degli Studi di Padova, (DAMA2021), Ministero dell'Università e della Ricerca (NEST Mission 4 Component 2 Investment 1.3 – Notice N. 341).

Conflicts of Interest

The authors declare that they have no known competing financial interests or personal relationships that could have appeared to influence the work reported in this article.

Data Availability Statement

The data that support the findings of this study are available from the corresponding author upon reasonable request.

References

1. A. Banerjee, B. Ziv, Y. Shilina, E. Levi, S. Luski, and D. Aurbach, "Single-Wall Carbon Nanotube Doping in Lead-Acid Batteries: A New Horizon," *ACS Applied Materials & Interfaces* 9 (2017): 3634–3643, https://doi.org/10.1021/acsami.6b13377.

2. M. Rodríguez-Gómez, J. Campo, A. Orera, et al., "Operando Analysis of the Positive Active Mass of Lead Batteries by Neutron Diffraction," *Journal of Power Sources* 591 (2024): 233822–233832, https://doi.org/10.1016/j.jpowsour.2023.233822.

3. B. Davoren and E. E. Ferg, "Spatially Resolved Characterization of the Porous Structure of Lead-Acid Battery Plates After Operation Using Micro-Computed Tomography," *Journal of Energy Storage* 74 (2023): 109542–109551, https://doi.org/10.1016/j.est.2023.109542.

4. J. Yin, H. Lin, J. Shi, et al., "Lead-Carbon Batteries Toward Future Energy Storage: From Mechanism and Materials to Applications," *Electrochemical Energy Reviews* 5 (2022): 2–32, https://doi.org/10.1007/s41918-022-00134-w.

5. X. Zhang, W. Chen, L. Yang, et al., "PEDOT-Coated Rice Husk-Based Activated Carbon: Boosting Lead-Acid Battery Performance," *Journal of Energy Storage* 90 (2024): 111771–111780, https://doi.org/10.1016/j.est.2024.111771.

6. Y. Zhang, C. gang Zhou, J. Yang, et al., "Advances and Challenges in Improvement of the Electrochemical Performance for Lead-Acid Batteries: A Comprehensive Review," *Journal of Power Sources* 520 (2022): 230800–230815, https://doi.org/10.1016/j.jpowsour.2021.230800.

7. N. Vangapally, T. R. Penki, Y. Elias, et al., "Lead-Acid Batteries and Lead–Carbon Hybrid Systems: A Review," *Journal of Power Sources* 579 (2023): 233312–233331, https://doi.org/10.1016/j.jpowsour.2023.233312.

8. O. Jhabli, M. Boutamart, E. M. El Mouchtari, et al., "New Insights Into Carbonaceous Materials and Lead/Carbon Composites in Lead Carbon Battery," *Journal of Energy Storage* 56 (2022): 106019–106041, https://doi.org/10.1016/j.est.2022.106019.

9. C. Ferels, N. Chaudhari, F. Agyapong-Fordjour, C. Buchanan, and P. P. Lopes, "Fundamental Benchmarking of the Discharge Properties of Negative Electrodes in Lead Acid Batteries," *Journal of Power Sources* 615 (2024): 235100–235110, https://doi.org/10.1016/j.jpowsour.2024.235100.

10. O. J. Dada, "Higher Capacity Utilization and Rate Performance of Lead Acid Battery Electrodes Using Graphene Additives," *Journal of Energy Storage* 23 (2019): 579–589, https://doi.org/10.1016/j.est.2019.04.004.

11. J. Kosacki and F. Dogan, "The Effect of Expanded and Natural Flake Graphite Additives on Positive Active Mass Utilization of the Lead-Acid Battery," *Journal of the Electrochemical Society* 168 (2021): 120540–120549, https://doi.org/10.1149/1945-7111/ac4188.

12. J. Jin, D. Jin, J. Shim, and W. Shim, "Enhancing Reversible Sulfation of PbO_2 Nanoparticles for Extended Lifetime in Lead-Acid Batteries," *Journal of the Electrochemical Society* 164 (2017): A1628–A1634, https://doi.org/10.1149/2.1291707jes.

13. W. Xu, L. Liu, M. Sajjad, J. Zhang, X. Yang, and Z. Mao, "From Traditional to Advanced: A Review on Carbon Addition as Key to Unlocking the Full Potential of Lead-Acid Batteries' Positive Electrode," *Journal of Energy Storage* 132 (2025): 118011–118024, https://doi.org/10.1016/j.est.2025.118011.

14. M. Cattelan, M. Mazzucato, and C. Durante, *Corrosion and Degradation in Fuel Cells, Supercapacitors and Batteries*, Springer Nature Switzerland, 2024). 195–217, "Corrosion in Pb-Acid Batteries—Recent Developments," https://doi.org/10.1007/978-3-031-57012-4_9.

15. M. Cattelan, G. Daniel, M. Mazzucato, et al., "Effect of Innovative Carbon Additives in the Positive Active Mass of Absorbent Glass Mat Lead Acid Battery," *Electrochimica Acta* 512 (2025): 145537–145548, https://doi.org/10.1016/j.electacta.2024.145537.

16. J. Shi, N. Lin, Y. Wang, D. Liu, and H. Lin, "The Application of Rice Husk-Based Porous Carbon in Positive Electrodes of Lead Acid Batteries," *Journal of Energy Storage* 30 (2020): 101392–101400, https://doi.org/10.1016/j.est.2020.101392.

17. P. T. Thong, D. J. Jeong, H. Seo, et al., "Cycle Performance Analysis of Lead–Carbon Electrode Under High-Load Conditions for Automotive Battery Applications," *Journal of Power Sources* 580 (2023): 233291–233302, https://doi.org/10.1016/j.jpowsour.2023.233291.

18. K. Yanamandra, D. Pinisetty, and N. Gupta, "Impact of Carbon Additives on Lead-Acid Battery Electrodes: A Review," *Renewable and Sustainable Energy Reviews* 173 (2023): 113078–113092, https://doi.org/10.1016/j.rser.2022.113078.

19. Y. Zhang, C. Zhou, X. Yan, H. Gao, K. Gao, and Y. Gao, "Synthesis of Nafion-Reduced Graphene Oxide/Polyaniline as Novel Positive Electrode Additives for High Performance Lead-Acid Batteries," *Electrochimica Acta* 466 (2023): 143045–143055, https://doi.org/10.1016/j.electacta.2023.143045.

20. G. Daniel, R. Trapula, A. Negretto, et al., *A Lead-Acid Battery Cell for Laboratory Activities*, 2024. EP24020242.4.

21. M. Kirchgeßner, R. Bußar, and H. Ramianpour, *Red Lead as a Key Factor for Higher Efficiency in the Formation of Lead-Acid Batteries*, 2023, PENOX Gmbh, https://www.penoxgroup.com/wp-content/uploads/White-Paper-Red_Lead_Formation_1_2023-12-01_Final.pdf.

22. D. Pavlov, *Lead-Acid Batteries: Science and Technology*. Elsevier, 2011).

23. S. Mandal, S. Thangarasu, P. T. Thong, S. C. Kim, J. Y. Shim, and H. Y. Jung, "Positive Electrode Active Material Development Opportunities Through Carbon Addition in the Lead-Acid Batteries: A Recent Progress," *Journal of Power Sources* 485 (2021): 229336–229356, https://doi.org/10.1016/j.jpowsour.2020.229336.

24. S. Zhang, L. Liu, M. Li, et al., "Polytetrafluoroethylene-Infused Dry Processed Enhancing Lead-Carbon Battery Performance," *Journal of Energy Storage* 132 (2025): 117819–117828, https://doi.org/10.1016/j.est.2025.117819.

25. J. Kosacki and F. Dogan, "The Effect of Various Graphite Additives on Positive Active Mass Utilization of the Lead-Acid Battery," *Journal of the Electrochemical Society* 168 (2021): 030513–030525, https://doi.org/10.1149/1945-7111/abe9c9.

26. H. Dietz, J. Garche, and K. Wiesener, "On the Behaviour of Carbon Black in Positive Lead-Acid Battery Electrodes," *Journal of Applied Electrochemistry* 17 (1987): 473–479, https://doi.org/10.1007/BF01084120.

27. Y. Wang, J. Wu, N. Lin, D. Liu, Z. Liu, and H. Lin, "Enabling Stable Cycling Performance With Rice Husk Silica Positive Additive in Lead-Acid Battery," *Energy* 269 (2023): 126796–126805, https://doi.org/10.1016/j.energy.2023.126796.

28. J. P. Meyers, R. C. de Guzman, S. W. Swogger, et al., "Discrete Carbon Nanotubes Promote Resistance to Corrosion in Lead-Acid Batteries by Altering the Grid-Active Material Interface," *Journal of Energy Storage* 32 (2020): 101983–101994, https://doi.org/10.1016/j.est.2020.101983.

29. L. Ren, W. Zhu, S. Li, et al., "Bifunctional Additive: Lead Dioxide Nanoparticle-Doped Graphene Oxide Composites for the Preparation and Performance Study of Positive Electrodes in Lead-Carbon Batteries," *Colloids and Surfaces A: Physicochemical and Engineering Aspects* 676 (2023): 132303–132317, https://doi.org/10.1016/j.colsurfa.2023.132303.

Supporting Information

Additional supporting information can be found on online in supporting information section. **Supporting Fig. S1:** (a) Weight loss of each LAB and (b) saturation degree of each cell's AGM separator during the formation processes. **Supporting Fig. S2:** PbO_2 content present in PAM after formation. **Supporting Fig. S3:** SEM images of standard (a) and positive electrodes modified with carbon additives: Graphite (b) and CB (c). **Supporting Fig. S4:** C_{20} curves related to LABs for 50% DoD tests (a) and WC tests (b and c). Specifically, (b) and (c) represented, respectively, the curves of the 2nd and 3rd C_{20} sequence related to LABs for WC tests. **Supporting Fig. S5:** 1st (a) and 2nd (b) CCA sequence curves related to LABs for WC tests. **Supporting Table S1:** The table represents the values of the physicochemical and electrochemical properties of the carbon additives. **Supporting Table S2:** Table representing the composition of various PAMs after the formation and after 50% DoD test.